

## Wave packet dynamics of $K_2$ attached to helium nanodroplets

P. Claas<sup>1</sup>, G. Droppelmann<sup>1</sup>, C. P. Schulz<sup>2</sup>, M. Mudrich<sup>3</sup>, F. Stienkemeier<sup>3</sup>

<sup>1</sup>Fakultät für Physik, Universität Bielefeld, 33615 Bielefeld, Germany

<sup>2</sup>Max-Born-Institut, Max-Born-Strasse 2a, 12489 Berlin, Germany

<sup>3</sup>Physikalisches Institut, Universität Freiburg, 79104 Freiburg, Germany

E-mail: mudrich@physik.uni-freiburg.de

**Abstract.** The dynamics of vibrational wave packets excited in  $K_2$  dimers attached to superfluid helium nanodroplets is investigated by means of femtosecond pump-probe spectroscopy. The employed resonant three-photon-ionization scheme is studied in a wide wavelength range and different pathways leading to  $K_2^+$ -formation are identified. While the wave packet dynamics of the electronic ground state is not influenced by the helium environment, perturbations of the electronically excited states are observed. The latter reveal a strong time dependence on the timescale 3–8 ps which directly reflects the dynamics of desorption of  $K_2$  on the helium droplets.

PACS numbers: 36.40.-c, 32.80.Qk

## 1. Introduction

The advent of femtosecond (fs) spectroscopy has allowed the visualization of the nuclear motion in molecular systems in "real-time", delivering new insight into the nature of the chemical bond and of the dynamics of chemical reactions [1, 2, 3, 4]. In femtosecond pump-probe experiments this visualization relies on the creation and interrogation of vibrational wave packets, i. e. coherent superpositions of vibrational states excited by the fs laser pulse. Fs pump-probe spectroscopy has become a widely-spread method providing complementary information to spectroscopy in the frequency domain because fast dynamical processes are often directly accessible.

Besides fs studies of molecules prepared in the gas phase, the real-time spectroscopy of molecules isolated in inert noble-gas matrices is an active field of research. On the one hand, matrix isolated molecules display a large variety of many-body phenomena such as solvational shifts of electronic states, electron-phonon coupling, matrix induced electronic and vibrational relaxation and decoherence, reduced dissociation probability ("caging effect"), excimer and exciplex formation, charge recombination [5]. On the other hand, these conceptually simple model systems can still be handled theoretically.

The field was pioneered by Zewail and co-workers using  $I_2$  as a molecular probe and varying the structural properties of the solvent environment from gas [6], over clusters [7] and liquid [8] to solid [7]. For example, in experiments with  $I_2$  in Ar clusters Liu and coworkers found that the coherent wave packet motion can survive the dissociation and matrix-induced recombination process [7]. Schwentner and coworkers have extended real-time studies to halogen molecules ( $I_2$ ,  $Cl_2$ ,  $Br_2$ ,  $CF_3$ ) in rare gas matrices, adding several new aspects in this kind of studies [9, 10, 11, 12]. Besides,  $Hg_2$  has been investigated in a cryogenic Ar matrix [13]. Conservation of vibrational coherence during a few picoseconds despite matrix induced electronic relaxation was observed. Due to the difficulty of implanting impurities into liquid helium, no real-time measurements with molecules in bulk liquid or solid helium have been reported until now. However, femtosecond laser-induced ionization of liquid helium and the subsequent preparation of  $He_2$  excimers in superfluid He has been reported [14]. Recently, electronic coherence relaxation of  $I_2$  in helium and other gases has been measured by fs photon echo [15].

Among the first molecules to be studied by fs spectroscopy in the gas-phase were alkali dimers [16, 17, 18, 19, 20, 21, 22]. Cold alkali dimers are easily prepared in a molecular beam and strong electronic transitions are well accessible by common fs laser sources. The potassium dimer  $K_2$  has been studied in detail in a series of one and two-color experiments demonstrating the propagation of vibrational wave packets in the ground state and in different excited states [19, 20, 23, 24, 25, 26, 27]. By varying the excitation laser wavelength and intensity, different pathways leading to ionization were identified. In addition, more subtle effects were studied such as the effect of spin-orbit coupling on the nuclear dynamics in the isotopomer  $^{39,39}K_2$  which is absent in  $^{39,41}K_2$  [23]. Visualizing the time evolution of vibrational frequencies using spectrograms was found to be useful for identifying transient phenomena such as fractional revivals in one-color

pump-probe scans which are absent in the case of two-color two-photon ionization [24].

In this work we present the first fs experiments probing wave packet propagation of molecules attached to superfluid helium nanodroplets. Today, helium nanodroplets are widely applied as a nearly ideal cryogenic matrix for spectroscopy of embedded molecules and as nanoscopic reactors for building specific molecular complexes [28, 29]. Alkali atoms and molecules represent a particular class of dopant particles due to their extremely weak binding to helium droplets with binding energies on the order of  $10\text{K}$  ( $7\text{cm}^{-1}$ ). From both theory and experiment it is known that alkali dimers reside in bubble-like structures on the surface of helium droplets [30, 31, 32]. Therefore, spectroscopic shifts of the electronic excitation spectra of alkali dimers are in the range of only a few  $\text{cm}^{-1}$  with respect to the gas phase [33, 32, 34, 35, 36]. Upon electronic excitation, alkali atoms and molecules mostly desorb from the droplets as a consequence of evaporation of helium atoms after energy deposition in the helium droplet [37, 38, 39]. The time scale for the desorption process is largely unknown. Solely in an early time-resolved study the desorption time of an alkali-helium excimer formed upon electronic excitation is estimated to be much shorter than the fluorescence lifetime [40].

Recently, the dynamics of photodissociation of molecules inside helium droplets has been studied both theoretically and experimentally. In Ref. [41], photodissociation of  $C_2$  embedded in helium clusters is studied by numerical simulation revealing reduced caging effects due to quantum properties of helium. The translational dynamics of  $CF_3$  in liquid helium was investigated experimentally by photodissociation of  $CF_3I$  dissolved in helium droplets [42]. Using ion imaging techniques, the velocity distribution of the fragments escaping from the droplets was found to be considerably shifted to lower speeds. This behavior was successfully modeled assuming binary collisions with helium atoms. The photoionization dynamics of aniline doped helium droplets was investigated by photoelectron spectroscopy [43]. In these experiments, droplet-size dependent lowering of the ionization threshold upon solvation was found.

Due to their weak coupling to the surrounding helium environment alkali dimers on helium droplets can be viewed as an intermediate system between free molecules and molecules isolated in conventional cryogenic matrices. The wave packet propagation is expected to be only weakly perturbed and new dynamical phenomena resulting from the desorption of the dimers upon fs excitation are observable. The highly quantum nature of superfluid  $^4\text{He}$  droplets vs. normal fluid  $^3\text{He}$  droplets may affect the coupling of the wave packet motion to the droplet [44, 45]. Moreover, exotic high-spin molecules and complexes formed on He droplets can be studied in real time [34, 46, 47]. The wave packet dynamics of  $Na_2$  in the lowest triplet state  $b^3_{u^+}$  will be presented in a separate paper.

## 2. Experimental

The experimental setup consists of three main parts, as illustrated in Fig. 1: A molecular beam line for  $K_2$ -doped helium droplets, an optical system to produce time delayed

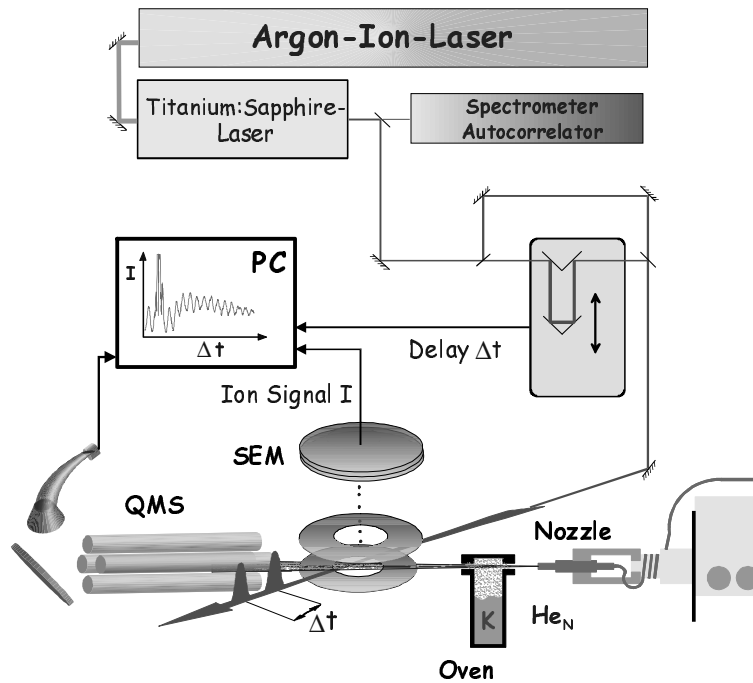


Figure 1. Schematic illustration of the experimental setup.

femtosecond laser pulses and a mass selective detection unit. The beam line consists of three differentially pumped vacuum chambers. In the first chamber the helium droplet beam is produced by condensation of helium gas (purity 99.9999%) in a supersonic expansion from a cold nozzle with a diameter  $d = 10 \text{ }\mu\text{m}$  into vacuum. At a nozzle temperature  $T = 19 \text{ K}$  and a stagnation pressure  $p = 50 \text{ bar}$  the droplets contain about 5000 atoms. By varying the temperature of the nozzle the average size of the droplets can be changed. To maintain a background pressure of  $10^{-3} \text{ mbar}$  we use a 8000 l/s oil diffusion pump backed up by a roots and rotary vane pump.

The beam enters the second chamber through a skimmer with an aperture of 400  $\mu\text{m}$  diameter. There the droplets pass a heated cell where they successively pick up two potassium atoms. Due to their high mobility on the superfluid helium droplets the picked-up atoms bind together to form dimers which are weakly bound in a dimple on the surface of the the helium nanodroplets. Collisional as well as binding energy is dissipated by the helium droplet through evaporation of helium atoms, which may cause the desorption of the alkali dimers from the droplets. Since the amount of internal energy released upon formation of ground state ( $X^1 \sigma_g^+$ ) dimers greatly exceeds the one released upon formation of dimers in the lowest triplet state  $a^3 \sigma_u^+$ , the later has a higher chance to remain attached to the droplet. This leads to an enrichment of the droplet beam with high-spin dimers and clusters compared to covalently bound systems [34, 47]. Nevertheless singlet ground state alkali dimers on helium droplets have been studied [32, 36]. The alkali-helium droplet complex eventually equilibrates at the terminal temperature of pure helium droplets of 380 mK. Thus, only the lowest

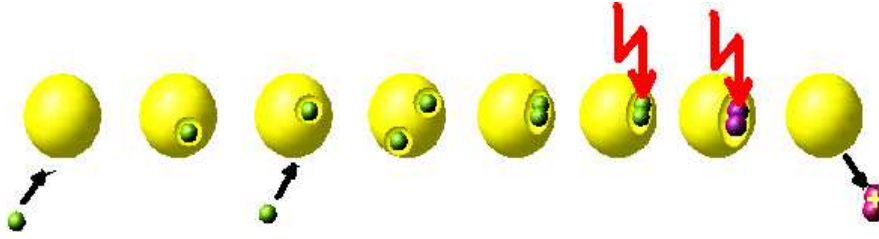


Figure 2. (Color online) Schematic illustration of the time sequence of the experiment. Successive pick-up of two alkali atoms by the helium droplet is followed by formation of a dimer. The later is excited by the pump pulse and ionized by the probe pulse.

vibrational state  $v^0 = 0$  and a few rotational states are populated which provides well-defined starting conditions for a pump-probe experiment. The number of collisions of the droplets with free dopant atoms inside the vapor cell is controlled by the oven temperature. Given the light distance of the droplets of 1 cm inside the vapor cell the potassium reservoir is heated to a temperature  $T = 410$  K to achieve highest probability for pick-up of two dopant atoms per droplet.

In the third vacuum chamber the doped droplet beam is intersected by the laser beam at right angle. The femtosecond laser pulses are generated by an  $Ar^+$ -laser pumped Ti:Sapphire laser (Tsunami, Spectra-Physics) at 80 MHz repetition rate and at an average power output between 1.2 and 1.4 W depending on the wavelength. This corresponds to a pulse energy of about 16 nJ. The pulses have a duration of 110 fs and a spectral bandwidth of  $135 \text{ cm}^{-1}$  (FWHM).

The laser beam is sent through a Mach-Zehnder interferometer to split the pulses into two time delayed pump and probe parts with equal intensity. The time delay is controlled by a commercial translation stage (PI M 531D G) having 0.225 fs as the smallest time increment. The collinear pulse pairs are then focused into the doped helium droplet beam using a lens of 150 mm focal length. The interaction volume is located inside the formation volume of a quadrupole mass spectrometer to mass selectively detect the photoions. We estimate the intensity of the laser light at the crossing point to be  $0.5 \text{ GW/cm}^2$  which corresponds to moderate intensity also used in the experiments reported in Refs. [19, 27]. The time sequence of the experiment is illustrated schematically in Fig. 2.

### 3. Pump-probe-spectroscopy of $K_2$

The one-color pump-probe experiments reported in this work are carried out in the wavelength region  $\lambda = 780 - 850 \text{ nm}$ . The excitation scheme leading to wave packet motion and subsequent ionization is illustrated in Fig. 3 using the gas-phase potentials from Refs. [48, 49]. The relevant potential energy curves are the ground state  $X^1 \text{ }^+ \text{ }_g$ , the first excited state  $A^1 \text{ }^+ \text{ }_u$ , the doubly excited state  $2^1 \text{ }_g$  and the ground state of the ion  $K_2^+$ ,  $X^2 \text{ }^+ \text{ }_g$ . The arrows indicate the excitation pathway leading to photoionization of

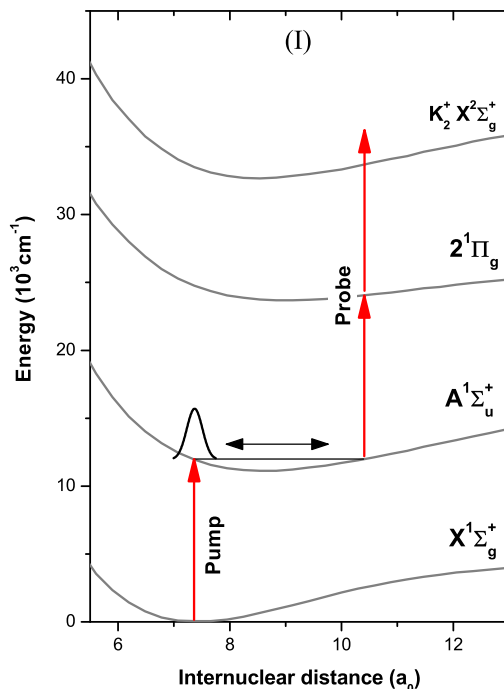


Figure 3. (Color online) Potential energy surfaces of neutral  $K_2$  and of  $K_2^+$  populated in the femtosecond pump-probe experiment. The arrows indicate pump and probe transitions for  $\lambda = 833 \text{ nm}$ .

$K_2$  at  $\lambda = 833 \text{ nm}$ . Starting from the vibrational ground state  $X^1\Sigma_g^+, v^0 = 0$ , absorption of one photon from the pump pulse creates a coherent superposition of ca. 5 vibrational states around  $v^0 = 12$  in the A-state at the classical inner turning point. The vibrational wave packet then propagates outwards and is transferred to the ionic state in a two-photon step via the intermediate resonant state  $2^1\Pi_g$  according to the resonance condition that photon energy equals the difference in potential energies of A and  $2^1\Pi_g$  states. It is essential to note that the  $2^1\Pi_g$ -state opens a Franck-Condon (FC) window for resonance enhanced ionization around a well-defined internuclear distance and therefore filters out the wave packet dynamics in the A-state [19]. Thus, the measured photoionization yield shows an oscillatory structure corresponding to the vibrational motion of the molecules (cf. Figs. 5, 6). This oscillation has a well-defined phase at zero delay times. At 833 nm the resonance condition is fulfilled at the outer turning point of the A-state. Thus, the time between wave packet creation and ionization roughly equals half a period of the wave packet oscillation and the detected signal has a phase  $\frac{A}{833}$ .

The described scheme at 833 nm is particularly favorable for several reasons. First, significant population of the  $2^1\Pi_g$ -state during the pump-pulse is suppressed because the  $2^1\Pi_g \leftarrow A$  transition is stronger than the  $A \leftarrow X$  transition [19]. This leads to pure (1+2)-photon excitation without contributions of (2+1)-photon transitions. Second, the outer

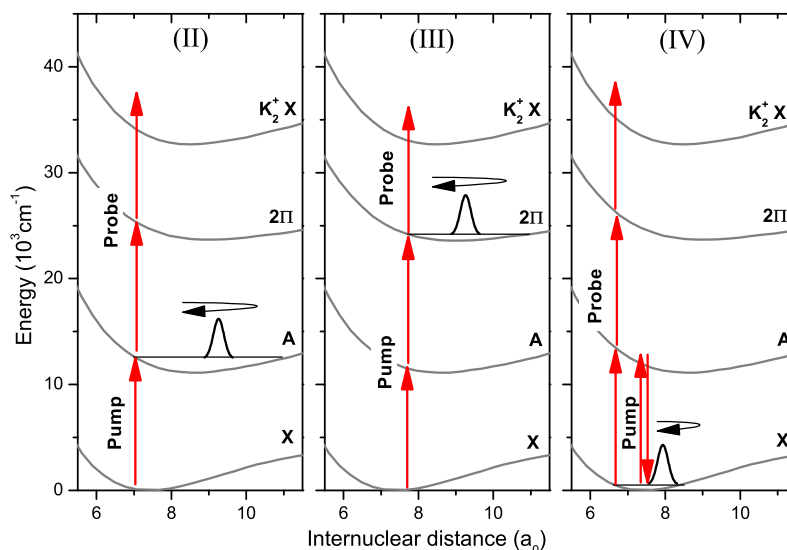


Figure 4. (Color online) Schematic illustration of different pump-probe mechanisms leading to photoionization of  $K_2$  (see text).

tuning points on the potential curves of the A and the X-state coincide. Therefore the FC factors for the A  $\rightarrow$  X transition is optimal at this wavelength [24]. Moreover, since the dynamics in the A-state is sampled at the turning point the detected oscillation directly reflects the nuclear dynamics [27].

Besides the described ionization scheme (type I) in the  $K_2$  experiments, the following alternative pathways are depicted in Fig. 4:

Type II: Wave packet excitation in the A-state. The transition to the ionic state takes place at the inner turning point, which results in a phase  $\frac{\pi}{2}$ . This scheme applies to the excitation at 780 nm.

Type III: Wave packet excitation in the  $2\Pi$ -state by absorption of two photons from the pump pulse. Ionization occurs by one-photon step during the probe pulse. This scheme is active at 780–800 nm.

Type IV: Wave packet excitation in the X-ground state by resonant impulsive stimulated Raman scattering (RISRS) during the pump pulse [20]. Transition to the ionic state is achieved by absorption of three photons from the probe pulse. This scheme applies to the excitation at 780–820 nm.

Around 850 nm, the excitation proceeds similarly to the type III scheme but involving the doubly excited state  $4^1_g^+$  instead of the  $2\Pi$ -state. Which one of the mentioned schemes is active, depends on the laser wavelength, intensity and polarization. For example in the one-color pump-probe experiments with  $K_2$  in a molecular beam reported by Nicole et al. [27], it was shown that type I is the dominant process in

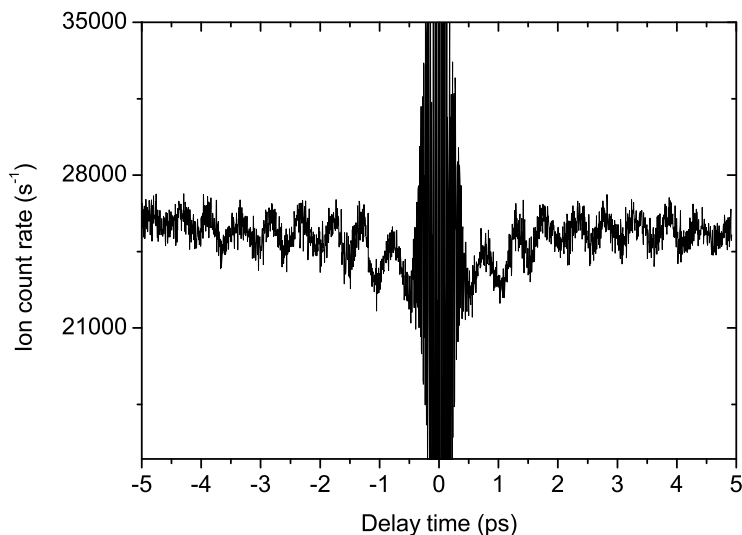


Figure 5. Raw  $K_2^+$  ion signal after pump-probe photoionization of  $K_2$  on helium nanodroplets as a function of delay time between pump and probe pulses recorded at  $\lambda = 810$  nm.

the wavelength range  $\lambda = 837 - 816$  nm, whereas at  $\lambda = 800 - 779$  nm type III also contributes. At  $\lambda = 779$  nm the observed transient was best reproduced by a sum of processes of type II and III. By increasing the laser intensity up to  $5 \text{ GW/cm}^2$ , it was shown that RISRS (type IV) significantly contributes, which gives a parameter to control the specific ionization pathway [20]. A different method for generating a wave packet in the ground state was studied using a two-color pump-dump-probe scheme involving the B-state [26]. In that work, the population of the ground state wave packet was controlled by varying the pump-dump delay and to a limited extent by varying the pump and dump laser wavelengths. Recently, Brixner et al. have shown that laser polarization opens an additional level of quantum control over the ionization mechanism. By altering the mutual polarization of pump and probe pulses using an optimal control scheme they were able to selectively enhance type I or type III transitions.

A typical real-time pump-probe spectrum of  $K_2$  attached to helium nanodroplets recorded at the mass of the  $^{39;39}K_2^+$  dimer at  $\lambda = 820$  nm is exemplified in Fig. 5. The signal is nearly symmetric with respect to the delay time zero which results from the almost identical pump and probe pulses interchanging their roles at time zero. Within the delay time window  $\pm 0.5$  ps the ion signal displays fast oscillations due to the autocorrelation of pump and probe pulse. This time interval is masked out in the further data analysis. For longer delay times, the ion signal features an oscillation on the ps time scale reflecting the wave packet dynamics. This oscillation is biased by a large background ion count rate which reduces the contrast to about 10%. The



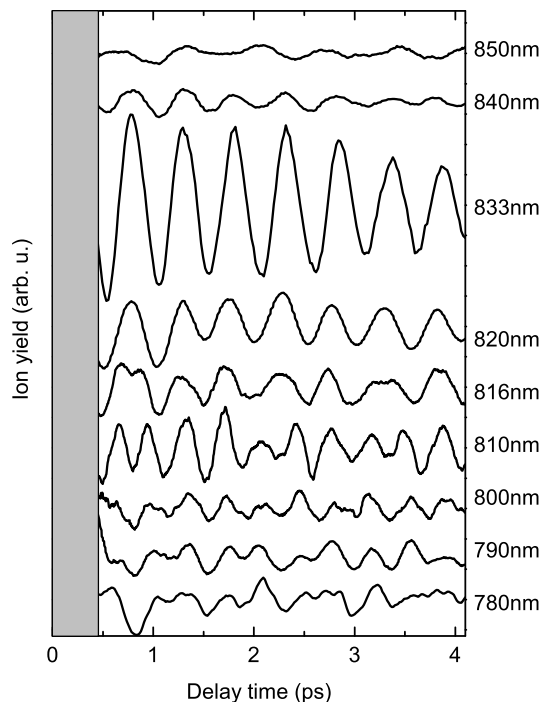


Figure 6. Processed pump-probe scans of  $K_2$  on helium nanodroplets for various excitation laser wavelengths.

background ion rate results from 3-photon ionization (3PI) of  $K_2$  during the pump or the probe pulse. A second background contribution comes from  $K_2$  dimers interacting with more than one pump-probe pulse pair as they fly through the laser focus. Due to the short period between two consecutive pump-probe pulse pairs of 12.5 ns (1/80 MHz) and the comparable 10 ns lifetime of the excited states, the illuminated  $K_2$  beam always contains a portion of already excited dimers.

In addition to the constant background another prominent feature shown in Fig. 5 is the increase of the ion signal during the first 3 ps. This is due to potassium clusters  $K_{N>2}$  formed on the helium droplets being photoionized and partially fragmenting into  $K_2^+$  fragment ions. Thus the fragmentation dynamics of alkali clusters is also accessible in our experiments but will be discussed in a separate paper. In order to prepare the data for Fourier transformation (FT) a band-pass filter is applied which suppresses the constant offset and slow variations as well as high frequency noise.

The processed experimental transient ion signals are summarized in Fig. 6 for short delay times 0–4 ps. As expected from the gas-phase, the most prominent oscillation occurs at  $\lambda = 833$  nm. Clearly, the oscillation amplitude is damped within the shown time interval. As the wavelength decreases the amplitudes quickly drop and a new higher frequency component appears which is most apparent at  $\lambda = 810$  nm. For even

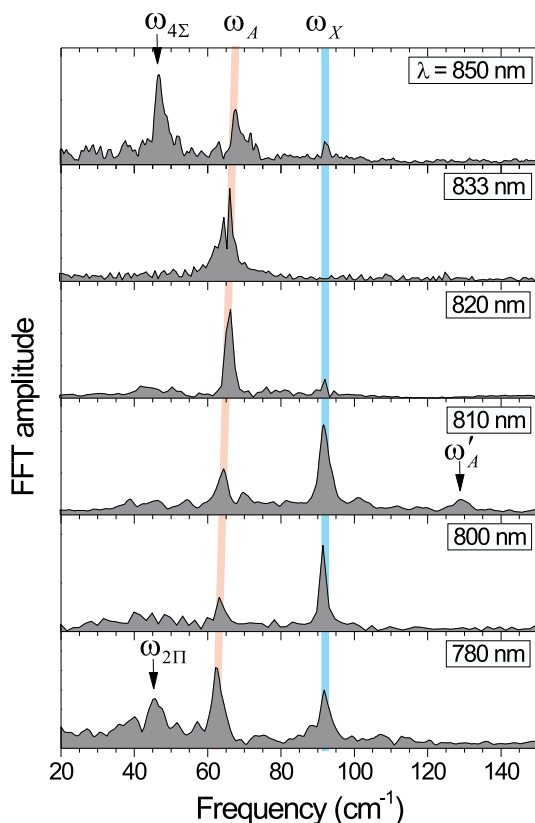


Figure 7. (Color online) Fourier transforms of experimental pump-probe scans at different laser wavelengths. The arrows and the colored straight lines indicate different frequency components.

smaller wavelengths, the transients feature a more complicated structure, indicating that more than one frequency component contributes. At  $\lambda = 850$  nm, the ionization trace is modulated by a slow oscillation with a rather weak amplitude. This oscillation has the opposite phase as the one observed at  $\lambda = 833$  nm.

In order to obtain more quantitative information about the exact frequencies and relative amplitudes of the contributing frequency components the pump-probe traces are Fourier transformed in the entire recorded delay time interval and plotted in Fig. 7. For the sake of clarity, the spectra are individually normalized to their maxima. One clearly distinguishes two characteristic frequencies which appear in all spectra. The frequency  $\omega_X = 92.1(7)$   $\text{cm}^{-1}$  matches the gas-phase vibrational constant  $\omega_e = 92.4$   $\text{cm}^{-1}$  of the ground state  $X^1_g$  [48]. Thus, a wave packet composed of the vibrational states  $v^0 = 0; 1$  is excited by R-IRIS (type IV transition). This type of ionization process was observed in Refs. [19, 20] in one-color experiments. In a two-color pump-dump-probe experiment wave packets around  $v^0 = 1; 2$  were excited leading to a level spacing  $\omega_X(1;2) = 91.5$   $\text{cm}^{-1}$  [26]. As expected for R-IRIS,  $\omega_X$  does not display any change with

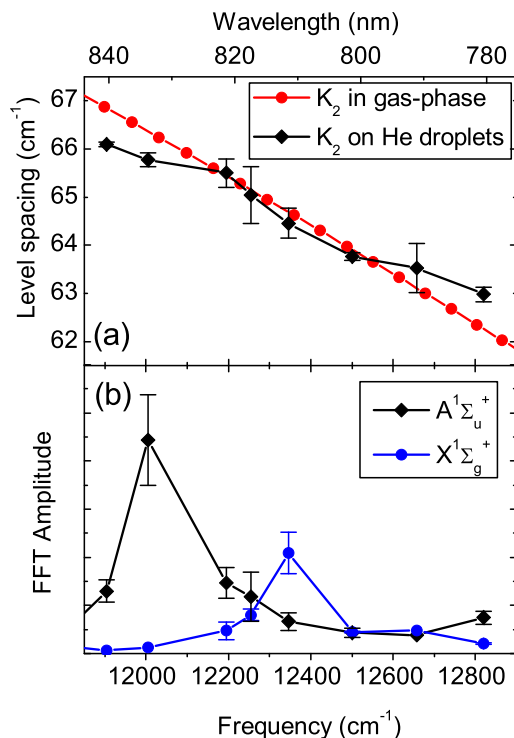


Figure 8. (Color online) (a) Oscillation frequencies of wave packets in the A-state of  $K_2$  attached to helium droplets vs. gas-phase values from Ref. [49]. (b) Relative amplitudes of the FT components  $\nu_A$  and  $\nu_X$  as a function of laser frequency.

varying laser wavelength. Moreover, no significant frequency shift due to the interaction with the helium droplet is observed. This result is not surprising when comparing to vibrational spectroscopy of molecules inside the droplets. Vibrational shifts typically lie in the range  $0.1 - 2 \text{ cm}^{-1}$  [28]. Since alkali dimers reside on the surface, even smaller shifts are expected.

The frequency component in the range  $64-66 \text{ cm}^{-1}$  belongs to the vibration in the A-state. It clearly shifts to higher values with increasing laser wavelength. This results from the anharmonicity of the A-state potential: As the excitation wavelength decreases higher vibrational levels, having a narrower energy spacing, are populated. The frequencies  $\nu_A$  obtained from FT of the first 7 ps are plotted in Fig. 8 (a). These frequencies are average values of level spacings of about 5 vibrational levels which lie inside the spectral profile of the fs laser. In order to compare this result to unperturbed  $K_2$  dimers, the corresponding average level spacings are calculated from experimental data from Ref. [49] which are plotted as full circles in Fig. 8 (a). For example the value close to  $\lambda = 810 \text{ nm}$  ( $12350 \text{ cm}^{-1}$ ) is calculated as the average of two level spacings,  $(G(v^0+1) - G(v^0-1))/2$ , for  $v^0 = 18$ . Here,  $G(v^0)$  stands for the vibrational energy of level  $v^0$ . Without quantitatively analyzing the populations and the helium-induced shifts of

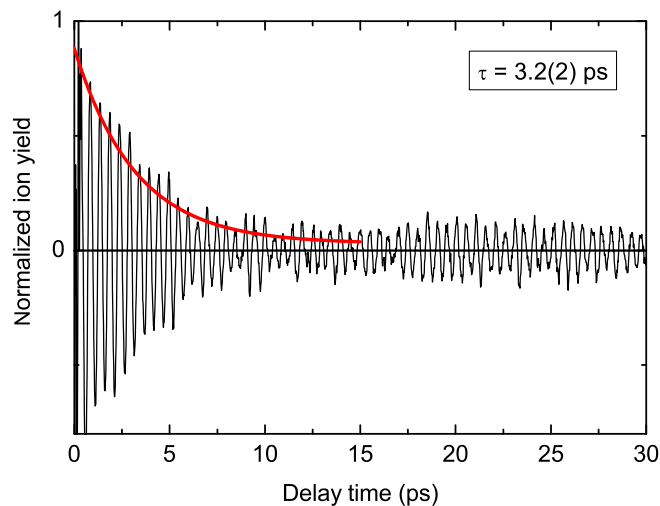


Figure 9. (Color online) Transient ionization signal of  $K_2$  attached to helium nanodroplets at 833 nm. The thick lines show the result of fitting an exponential decay function with constant offset to the absolute amplitude of the observed oscillation.

the  $v^0$ -levels, Fig. 8 (a) indicates a clear trend: In the wavelength range  $\lambda = 840 - 780$  nm the vibrational level spacings of  $K_2$  on helium droplets vary more slowly than the ones of free  $K_2$ . Thus, the helium droplet environment influences the shape of the potential curve of the A-state of  $K_2$  such that anharmonicity is reduced. Note that the frequencies obtained from FT of our data in the time interval 10 - 20 ps, i.e. when desorption is complete, agree with the calculated values within the error bars.

The amplitudes of the frequency components of X and A-states obtained from FT of the first 7 ps delay time are shown in Fig. 8 (b). The maxima are located around  $12350 \text{ cm}^{-1}$  (810 nm) and  $12000 \text{ cm}^{-1}$  (833 nm), respectively. Surprisingly, in the range 800-815 nm, the X-component dominates over the A-component, which strongly differs from the gas-phase observations at moderate laser intensities [19, 27]. According to [19, 27], wave packets in the X-state are not detected at moderate laser intensities due to the mismatch of the FC window for ionization determined by the  $2^2$ -state and the X-state wave packet. In the case of  $K_2$  on helium droplets, a well localized FC window appears in 3P I from the X-state. Because of the Pauli repulsion of the helium environment towards the alkali valence electrons and the induced change in the spatial valence electronic distribution upon electronic excitation, in particular the higher excited states are expected to evolve larger energy shifts. The results demonstrate that the helium-induced shifts of the potential energy curves significantly alter FC overlaps. In the following, several characteristic wavelengths are discussed in more detail.

833 nm The damped oscillation recorded at 833 nm is plotted for longer delay times in Fig. 9. In addition to the experimental data the result of fitting an exponential decay function with a constant offset to the absolute oscillation amplitude is represented as a thick line. The exponential drop by about one order of magnitude has a time constant  $\tau = 3.2(2)$  ps and the constant offset amounts to merely 5% of the initial amplitude. This initial amplitude decrease is not observed in gas-phase measurements [23, 27]. Generally, this dynamics can originate from two different mechanisms connected to the influence of the helium matrix. First, matrix-induced effects such as vibrational relaxation may lead to decoherence of the wave packet [50]. In this case, the  $K_2$  dimers are stuck to the helium surface and the coherent oscillation is damped and eventually completely vanishes. However, this is not the case in our experiment. Second, additional dynamics is introduced by the effect of desorption of  $K_2$  from the helium surface, leading to a transient perturbation of the wave packet motion. Finally, both of the mentioned effects may contribute to the observed dynamics. As discussed in more detail in the last section, we interpret the observed exponential drop as the effect of desorption of  $K_2$  from the helium nanodroplets. The distortion of the potential curves resulting from the interaction with the helium leads to an enhancement of resonant 3PI which vanishes as  $K_2$  moves away from the helium surface.

The FT spectrum at 833 nm shown in Fig. 7 clearly indicates that only one frequency component contributes to the wave packet dynamics. The oscillation period and phase during the initial exponential decay are found to be  $T_{A_1}^{833\text{nm}} = 507$  fs ( $\nu_{A_1} = 65.8 \text{ cm}^{-1}$ ) and the phase equals half the oscillation period ( $\phi_{A_1}^{833\text{nm}} = 0.99 \pi$ ,  $\approx 255$  fs). This confirms that at this wavelength  $K_2$  is ionized following the pathway of type I as in the gas-phase. At delay times exceeding the desorption time the oscillation period is reduced to  $T_{A_2}^{833\text{nm}} = 503$  fs ( $\nu_{A_2} = 66.3 \text{ cm}^{-1}$ ). This value is in good agreement with the gas phase measurements of Ref. [49]. In gas-phase measurements with  $^{39;39}K_2$  recording much longer scans, Rutz et al. were able to resolve by FT each frequency spacing between the vibrational levels contributing to the wave packet. At 833.7 nm it was found that the FT spectrum is dominated by two frequency components  $G(\nu^0) - G(\nu^0 - 1)$  and  $G(\nu^0 + 1) - G(\nu^0)$  for  $\nu^0 = 13$  due to spin-orbit coupling between the A-state and the  $b^3 \Sigma_u^-$ -state [23]. The center of gravity of the lines lies at about  $66 \text{ cm}^{-1}$  which is again in good agreement with our findings. This suggests that in our experiment a wave packet consisting of about 5 vibrational components around the  $\nu^0 = 13$  vibrational state is excited.

The remaining oscillation after the initial damping features a slow periodic modulation with a period of about 26 ps. The gas phase measurement with the isotomer  $^{39;39}K_2$  also shows a pronounced beat structure with a period of about 10 ps, induced by the two dominating components mentioned above. In the isotomer  $^{39;41}K_2$  spin-orbit coupling is not active in this region of the A-state potential [23]. In that case, the beat structure is less pronounced and more complicated with longer periods  $> 50$  ps, resembling more the one that we measure with  $^{39;39}K_2$  on helium droplets. The fact that the beating pattern after desorption does not precisely match the observed beating in the

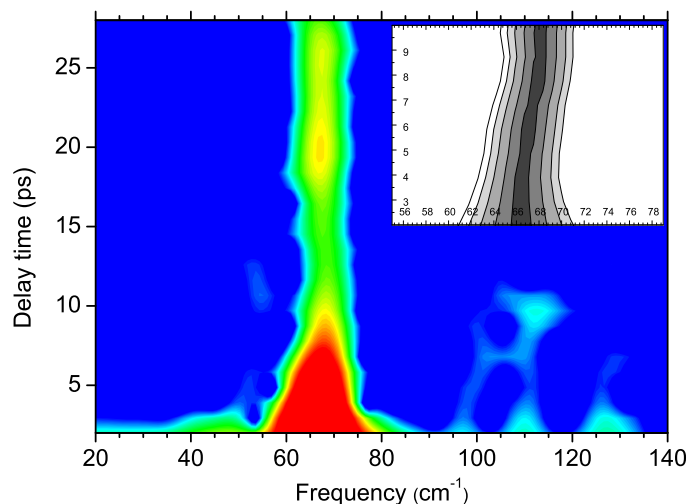


Figure 10. (Color online) Logarithmic contour plot of the spectrogram calculated from the pump-probe signals at the excitation wavelength  $\lambda = 833 \text{ nm}$ . The inset extracts the first 10 ps normalizing the data for each time step.

gas-phase measurements is not totally understood. Presumably, we account differences in the used pulse widths and shapes as well as differences in the wave packet formed under perturbed conditions for this discrepancy.

The evolution of  $\nu_A$  can be followed in real-time by Fourier transforming the data inside of a 3 ps time window which slides across the entire data set [24]. The resulting spectrogram is depicted in Fig. 10 as a contour plot with logarithmic scale. Naturally, the frequency resolution is reduced so that  $\nu_A^{833\text{nm}}(t_{\text{delay}})$  appears as a rather broad vertical band. The color scale goes from blue for low to red for high amplitudes of the Fourier components. Thus, the initial drop of the oscillation amplitude at  $\nu_A^{833\text{nm}} \approx 66 \text{ cm}^{-1}$  is visualized as intense red color which fades out at  $t_{\text{delay}} \approx 10 \text{ ps}$  and reappears at around  $t_{\text{delay}} \approx 20 \text{ ps}$  indicating the revival mentioned above. The time evolution of the amplitude of  $\nu_A^{833\text{nm}}$  obtained by averaging within a frequency interval  $55\text{--}80 \text{ cm}^{-1}$  is plotted in Fig. 11 (a). Obviously, the data reproduce the decreasing oscillation amplitude at  $833 \text{ nm}$  as reflected by the  $\nu$  curve from Fig. 9 (solid line).

The shifting of the frequency  $\nu_A^{833\text{nm}}$  is clearly visible in Fig. 10 as a deviation of the green band from a vertical line. In particular, during the first 10 ps in which the oscillation amplitude decreases exponentially,  $\nu_A^{833\text{nm}}$  shifts roughly linearly to higher frequencies from  $65.8 \text{ cm}^{-1}$  to  $66.3 \text{ cm}^{-1}$ , as depicted in the inset of Fig. 10 using a different color scaling. This frequency shift is attributed to the effect of diminishing perturbation of  $K_2$  by the helium droplet as it desorbs from the droplet. Presumably, the perturbation of the A-state potential by helium vanishes as  $K_2$  desorbs from the helium surface thereby shifting the vibrational frequencies back to their gas-phase values.

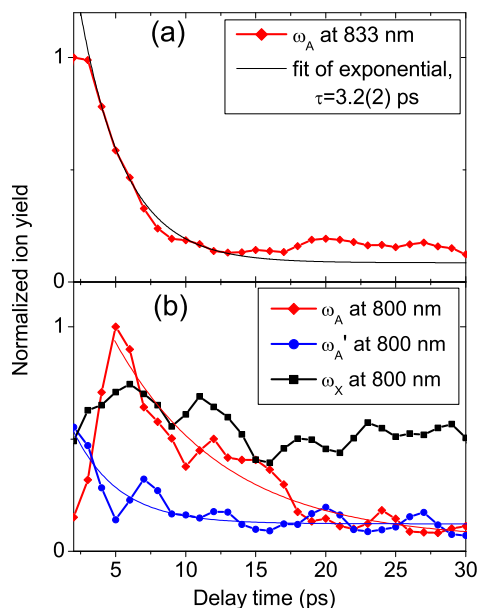


Figure 11. (Color online) Time evolution of the relative amplitudes of different frequency components at  $\lambda = 833\text{ nm}$  (a) and  $\lambda = 800\text{ nm}$  (b).

820 nm The transient ionization signal at 820 nm shown in Fig. 6 resembles the one at 833 nm in the way that it features a pronounced oscillation which is damped during the first 8 ps. The period  $T_A^{820\text{nm}} = 520\text{ fs}$  ( $\nu_A^{820\text{nm}} = 64.1\text{ cm}^{-1}$ ) and phase  $\phi_A^{820\text{nm}} = 0.96$  (250 fs) again indicate wave packet propagation in the A-state (type I scheme). This result is somewhat surprising since the corresponding gas-phase signals are quite different [27]. In the gas phase, the maxima of the oscillation are split into two peaks of different amplitudes, which is well described by the wave packet moving twice through the FC window in each round trip. This is due to the fact that at 820 nm the outer turning point of the  $2^-$ -state (defining the FC window) no longer coincides with the one in the A-state but is shifted to smaller internuclear distance. This seems not to be the case when  $K_2$  is attached to helium droplets. This can be explained by either the shape of the A-state or of the  $2^-$ -state being influenced by the helium such that the FC overlap localized at the outer turning points is maintained down to a wavelength  $\lambda = 816\text{ nm}$ . Since the vibrational frequencies in the A-state are only weakly perturbed (Fig. 8 (a)), most likely the  $2^-$ -state is bent up to higher energies in the outer region of the potential well similarly to the caging-effect of rare-gas matrices on the potential curves of  $I_2$  [9]. Thus the the FC-window is shifted to shorter internuclear distances.

810 nm The new frequency component showing up at decreasing excitation wavelengths is most apparent at  $\lambda = 810\text{ nm}$ . We find a period  $T_X^{810\text{nm}} = 364\text{ fs}$  corresponding to  $\nu_X^{810\text{nm}} = 91.7(8)\text{ cm}^{-1}$  which is in good agreement with the gas-phase vibrational constant  $\nu_e = 92.4\text{ cm}^{-1}$  of the ground state  $X^1_g$  [48]. The phase is

found to be  $\tau_X^{810\text{nm}} = 1.3$  (245 fs). Thus, we identify a type IV ionization sequence in this wavelength region. This finding quite significantly differs from the gas-phase results. According to [19, 27] no wave packet dynamics in the X-state is observed. Instead, wave packet excitation in the 2-state contributes to an increasing extent at shorter wavelengths. In the gas-phase, Fourier analysis of the transients at 834 nm does reveal a frequency component corresponding to wave packet motion in the X-state. However the amplitude is negligible with respect to the A-state contribution [19, 23]. A dominating RIRS excitation was only observed at laser intensities exceeding the ones in our experiment by more than a factor 10 [20]. This again demonstrates the sensitivity of the population transfer and the produced wave packets on weak perturbations of the involved states and the corresponding FC overlaps.

In addition to  $!_X^{810\text{nm}}$  and  $!_A^{810\text{nm}}$  there is a third component  $!_A^{0810\text{nm}} = 128 \text{ cm}^{-1}$ . This frequency is interpreted in terms of the wave packet in the A-state being ionized via 2 distinct windows in the coordinate of internuclear distance. The FC window is situated at the outer turning point at  $\lambda = 833 \text{ nm}$  and at the inner turning point at  $\lambda = 780 \text{ nm}$ . Apparently, the transition between the two regimes takes place at  $\lambda = 810 \text{ nm}$ . The interpretation of  $!_A^{0810\text{nm}}$  being due to the coherent excitation of vibrational energy levels with  $v^0 = 2$  as it was observed in Ref. [24] seems unlikely in our case. The latter effect is a general feature depending only on the vibrational level spacing and the spectral width of the laser pulses. Therefore, a doubled frequency  $2!_A$  should appear in all FT spectra, which is not the case in our measurements. One should note here that the spectral width of the laser pulses in the experiments of Ref. [24] were larger by a factor of 1.6 than in our experiments.

The time evolution of frequencies  $!_X^{810\text{nm}}$ ,  $!_A^{810\text{nm}}$  and  $!_A^{0810\text{nm}}$  at  $\lambda = 810 \text{ nm}$  can be followed in the corresponding spectrogram in Fig. 12. The ground state component  $!_X^{810\text{nm}} = 92 \text{ cm}^{-1}$  is visible during the entire scan and does not reveal any significant frequency changes. The frequencies  $!_A^{810\text{nm}}$  and  $!_A^{0810\text{nm}}$ , however, are observable in the spectrogram only during the first 10 ps and do not display any revivals at later times. Again, this dynamics is associated with the  $K_2$  desorbing from the droplets upon electronic excitation. It is interesting to note that, in contrast to the amplitudes of components  $!_A^{810\text{nm}}$  and  $!_A^{0810\text{nm}}$ , no significant damping of the wave packet motion in the X-state excited by RIRS is observed. Hence, no significant desorption of  $K_2$  from the helium droplets occurs as long as only vibrational states of the electronic ground state X are redistributed. This observation agrees well with the picture of dopant molecules desorbing from the surface only due to strong evaporation caused by a sudden perturbation upon spatial expansion of the valence electronic distribution due to the laser induced transition [51]. The energy deposited into the droplet clearly shows up as intense blue-shifted sidebands when probing alkali dimer transitions by means of fluorescence absorption spectroscopy. By fitting an exponential decay function to the amplitudes of the components  $!_A^{810\text{nm}}$  and  $!_A^{0810\text{nm}}$  in the same way as illustrated in Fig. 11 (b) at  $\lambda = 800 \text{ nm}$  one obtains a time constant  $\tau_A^{810\text{nm}} = 6.6(5) \text{ ps}$  for both  $!_A^{810\text{nm}}$  and  $!_A^{0810\text{nm}}$ . [32, 34].



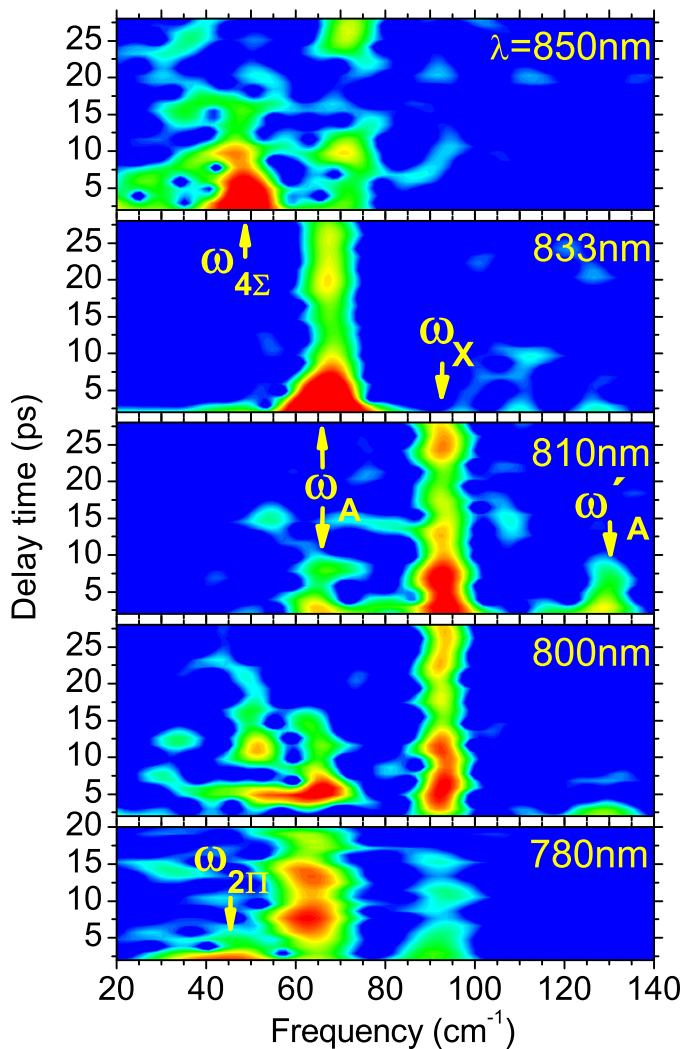


Figure 12. (Color online) Overview over the spectrograms at characteristic excitation laser wavelengths.

800 nm The spectrogram at the excitation wavelength  $\lambda = 800$  nm (Fig. 12) displays the time evolution of the frequency components  $\omega_X^{800\text{nm}}$ ,  $\omega_A^{800\text{nm}}$  and  $\omega_A^{0800\text{nm}}$ , as for  $\lambda = 810$  nm. The time evolution of the corresponding amplitudes is depicted in Fig. 11 (b). The ground state component  $\omega_X^{800\text{nm}}$  remains largely unchanged during the shown time interval. The slight increase in amplitude at  $t_{\text{delay}} = 22$  ps which is also observed at  $\lambda = 810$  nm may reflect a revival of the wave packet motion. The amplitudes of components  $\omega_A^{800\text{nm}}$  and  $\omega_A^{0800\text{nm}}$ , however, now behave differently than at  $\lambda = 810$  nm. While the weaker component  $\omega_A^{0800\text{nm}}$  at  $130$   $\text{cm}^{-1}$  disappears with a time constant  $\tau_A^{800\text{nm}} = 32(7)$  ps,  $\omega_A^{800\text{nm}}$  at  $65$   $\text{cm}^{-1}$  only reaches its maximum amplitude around

5 ps. The following decay has a time constant  $\tau_A^{800\text{nm}} = 8(1)$  ps.

This means that during the desorption process the FC window for the probe step into the ionic state is shifted. In the beginning, transitions take place at the outer turning point as well as at the inner turning point of the A-state potential. As the influence of the helium diminishes upon desorption, the FC-window shifts to the outer turning point. After desorption is complete, ionization of the A-state is suppressed. Thus a transition from the excitation scheme of type I to the one of type II is taking place at this wavelength for  $K_2$  on helium droplets. Besides the shift of the frequency  $\nu_A$  at  $\lambda = 833$  nm, the opening and closing of FC-windows observed at  $\lambda = 800$  nm is a clear indication for the dynamics induced by the desorption process of  $K_2$  on the helium droplets.

**780 nm** Around 780 nm, the recorded oscillation of the ion signal has a period changing from  $T_{A_1}^{780\text{nm}} = 529$  fs ( $\nu_{A_1}^{780\text{nm}} = 63$  cm<sup>-1</sup>) to the value observed in the gas phase,  $T_{A_2}^{780\text{nm}} = 537$  fs ( $\nu_{A_1}^{780\text{nm}} = 62.1$  cm<sup>-1</sup>), within the first 20 ps. The phase is found to be  $\phi_A^{780\text{nm}} = 0.1$  (28 fs). Thus, this wave packet motion occurs in the A-state according to the type II scheme, which is also observed in gas-phase experiments [27]. The changing oscillation period is again attributed to the desorption dynamics. However, in contrast to the behavior at 833 nm, in this case  $T_{A_1}^{780\text{nm}} < T_{A_2}^{780\text{nm}}$  as shown in Fig. 8. The amplitude of the component  $\nu_A^{780\text{nm}}$  evolves differently at 780 nm than at previously discussed wavelengths. From 0-8 ps it rises by a factor two and decays slowly at later times. The FC-window seems not to shift sufficiently during the desorption for significantly changing the detection efficiency of the A-state wavepacket. Presumably, this is due to the fact that the inner part of the  $K_2$  dimer potential where the transition takes place at this wavelength is less sensitive to small perturbations by the external environment.

Besides the dominating frequency component  $\nu_A^{780\text{nm}}$  the spectrogram of Fig. 12 displays the time evolution of  $\nu_X^{780\text{nm}} = 45$  cm<sup>-1</sup> and  $\nu_2^{780\text{nm}} = 92$  cm<sup>-1</sup>. The latter frequency reflects the wave packet motion excited in the 2 state by the transition sequence of type III. In the gas phase, this oscillation dephases within ca. 2 ps due to the anharmonicity of the potential. From fitting an exponential decay function to our data we find an exponential decay constant  $\tau_2^{780\text{nm}} = 1.4(2)$  ps, in agreement with the gas-phase observations. The ground state component  $\nu_X^{780\text{nm}}$  reveals a slow decrease which may however be due to dephasing as it is observed at  $\lambda = 800$  nm and  $\lambda = 810$  nm.

**850 nm** In the range of 850 nm the ionization transient displays a regular oscillation with a period  $T_4^{850\text{nm}} = 700$  fs ( $\nu_4^{850\text{nm}} = 48$  cm<sup>-1</sup>) and a phase  $\phi_4^{850\text{nm}} = 1.9$  (650 fs). We interpret this oscillation as wave packet motion in the  $4^1_g$ -potential detected by the type III scheme involving state 4 instead of 2. In quantum dynamics calculations of the ion yield at the excitation wavelength  $\lambda = 840$  nm, it was found that the state 4 is populated but only weakly contributes to the ion yield originating predominantly from the type I process [19]. Presumably the opposite is true as the wavelength increases

to  $\lambda = 850 \text{ nm}$ . The average vibrational splitting was found to be  $52 \text{ cm}^{-1}$  ( $\nu^0 = 33\text{--}38$ ) which roughly matches the oscillation frequency  $\omega_4^{850\text{nm}} = 48 \text{ cm}^{-1}$  measured in our experiment. As shown in Fig. 12, the component  $I_4^{850\text{nm}}$  evolves an exponential decay with a time constant  $\tau_4^{850\text{nm}} = 5.8(6) \text{ ps}$  which agrees with the calculated dephasing time due to anharmonicity [19]. The amplitude of the weaker ground state component  $I_X^{850\text{nm}}$  fluctuates around a constant value indicating vanishing perturbation of the ground state dynamics.

#### 4. Summary

The wavepacket motion observed by resonant and resonance-enhanced 3PI of  $K_2$  on helium nanodroplets at various excitation wavelengths displays a number of characteristic features as compared to analogous results of gas phase experiments. Let us summarize the observations giving information about the influence of the helium droplet on the wave packet dynamics. At  $\lambda = 833 \text{ nm}$ , the strong oscillation of the ion yield due to resonant 3PI is damped with a time constant  $\tau = 3.2(2) \text{ ps}$  but a constant long-lived oscillation persists. On the same timescale the frequency of the wave packet motion in the A-state shifts by  $0.5 \text{ cm}^{-1}$  from  $65.8 \text{ cm}^{-1}$  to the gas phase value,  $66.3 \text{ cm}^{-1}$ . At  $\lambda = 820 \text{ nm}$ , no splitting of the maxima in the ion transient due to inward-outward motion of the wave packet through the FC-window is measured contrary to gas phase observations. At  $\lambda = 810 \text{ nm}$ , enhanced RIRS is observed as opposed to negligible RIRS at moderate laser intensities in the gas phase. The frequency shift  $\Delta_A$  at  $\lambda = 780 \text{ nm}$  is comparable to the one at  $\lambda = 833 \text{ nm}$  but has opposite sign.

The transient effect of the helium environment appears most prominently in the wave packet dynamics observed according to the type I scheme. Here, the ionization efficiency depends sensitively on the outer part of the potential curve which is particularly affected by the interaction with the helium. This explains the strong amplitude damping and the shifting frequency at  $\lambda = 833 \text{ nm}$ . The ionization processes of type II to IV proceed via the inner part of the excited potential curves. Therefore the influence of the surrounding helium is expected to be less visible. In particular, the time varying perturbation by the helium as the  $K_2$  dimers desorb from the droplet surface causes different dynamics. As the ionization scheme gradually evolves from type I to type II for decreasing wavelengths  $\lambda = 833 \text{--}780 \text{ nm}$ , the competition of the two schemes is observable by the appearance and disappearance of the frequency components connected with the different schemes, as observed at  $\lambda = 800 \text{ nm}$ . Consequently, the amplitude of  $\Delta_A$  at  $\lambda = 780 \text{ nm}$  (type II process) displays only a weak variation with time.

In contrast to these findings, the wave packets excited by RIRS in the ground state experience no significant influence by the helium environment. The vibrational frequency remains unshifted with respect to the gas phase, and the amplitude of the detected wave packet motion in the ground state only weakly varies with time, presumably reflecting a revival structure. Since no change of the valence electronic

distribution occurs upon RISRS, only coupling of the vibrational excitation to the helium bath might induce perturbations of the wave packet motion. Since the latter is known to be much weaker than the interaction with the helium droplet upon electronic excitation, no significant perturbations are expected.

In order to draw more quantitative conclusions from our observations quantum dynamics simulations should be performed, introducing perturbed  $K_2$  potential curves to mimic the influence of the helium droplet. Also, the process of desorption of alkali atoms and molecules from helium droplets and, in particular, the impact on the nuclear wave packet dynamics, is largely unexplored by theory.

The experiments presented in this work clearly demonstrate that the influence of the helium matrix on the wave packet dynamics of  $K_2$  can be studied in real time using fs pump-probe spectroscopy. Surprisingly, this weak coupling quite dramatically alters the photoionization process which demonstrates the sensitivity of Franck-Condon factors on helium induced shifts of the potential energies. The time variation of the Franck-Condon windows and of oscillation frequencies converging to their gas phase values clearly reflects the dynamics of the process of desorption of the  $K_2$  dimers from the helium droplets, which proceeds on the timescale 3–8 ps.

#### Acknowledgments

Technical support with the laser system by V. Petrov and the help with producing spectrograms by S. Rutz is gratefully acknowledged. The work is financially supported by the DFG.

#### References

- [1] A. H. Zewail. *Journal of Physical Chemistry A*, 104:5660, 2000.
- [2] A. Zewail. *Femtochemistry*. World Scientific, Singapore, 1994, 1994.
- [3] J. Manz and L. Woste, editors. *Femtosecond Chemistry*. VCH, Weinheim, 1995.
- [4] M. Chergui, editor. *Femtochemistry*. World Scientific, Singapore, 1995.
- [5] V. A. Apkarian and N. Schwentner. *Chem. Rev.*, 99:1481, 1999.
- [6] C. Wan, M. Gupta, J. Baskin, Z. Kim, and A. H. Zewail. *Journal of Chemical Physics*, 106:4353, 1997.
- [7] Q. Liu, J.-K. Wang, and A. Zewail. *Nature*, 364:427, 1993.
- [8] C. Lienau and A. H. Zewail. *Chemical Physics Letters*, 222:224, 1994.
- [9] M. Bargheer, P. Dietrich, K. Donovan, and N. Schwentner. *Journal of Chemical Physics*, 111:8556, 1999.
- [10] M. Fushitani, N. Schwentner, M. Schroder, and O. Kuhn. *Journal of Chemical Physics*, 124:024505, 2006.
- [11] M. Gühr, H. Ibrahim, and N. Schwentner. *Physical Chemistry Chemical Physics*, 6:5353, 2004.
- [12] M. Bargheer, M. Y. Niv, R. B. Gerber, and N. Schwentner. *Physical Review Letters*, 89:108301, 2002.
- [13] C. R. Gonzalez, S. Fernandez-Auberti, and J. Echave. *Journal of Chemical Physics*, 116:3343, 2002.
- [14] A. V. Benderskii, R. Zadoyan, N. Schwentner, and V. A. Apkarian. *Journal of Chemical Physics*, 110:1542, 1999.

- [15] M. Comstock, V. V. Lozovoy, and Marcos Dantus. *Journal of Chemical Physics*, 119:6546, 2003.
- [16] J. M. Papanikolas, R. M. Williams, P. K. Leiber, J. L. Hart, C. B. Rink, S. D. Price, and S. R. Leone. *Journal of Chemical Physics*, 103:7269, 1995.
- [17] T. Baumert, M. G. Rosser, R. Thalweiser, and G. Gerber. *Physical Review Letters*, 67:3753, 1991.
- [18] T. Baumert, V. Engel, C. Meier, and G. Gerber. *Chemical Physics Letters*, 191:639, 1992.
- [19] R. de Vivie-Riedle, B. Reischl, S. Rutz, and E. Schreiber. *Journal of Physical Chemistry A*, 99:16829, 1995.
- [20] R. de Vivie-Riedle, K. K. Kobe, J. Manz, W. Meyer, B. Reischl, S. Rutz, E. Schreiber, and L. Woste. *Journal of Physical Chemistry A*, 100:7789, 1996.
- [21] G. Rodriguez and J. G. Eden. *Chemical Physics Letters*, 205:371, 1993.
- [22] V. Blanchet, M. A. Bouchene, O. Cabrol, and B. Girard. *Chemical Physics Letters*, 233:491, 1995.
- [23] Soeren Rutz, Regina de Vivie-Riedle, and Elmar Schreiber. *Physical Review A*, 54:306, 1996.
- [24] Soeren Rutz and Elmar Schreiber. *Chemical Physics Letters*, 269:9, 1997.
- [25] H. Schwörer, R. Pausch, M. Heid, V. Engel, and W. Kiefer. *Journal of Chemical Physics*, 107:9749, 1997.
- [26] R. Pausch, M. Heid, T. Chen, W. Kiefer, and H. Schwörer. *Journal of Chemical Physics*, 110:9560, 1999.
- [27] C. Nicole, M. A. Bouchene, C. Meier, S. Magnier, E. Schreiber, and B. Girard. *Journal of Chemical Physics*, 111:7857, 1999.
- [28] J. P. Toennies and A. F. V. Ilisov. *Angewandte Chemie*, 43:2622{2648, 2004.
- [29] Frank Stienkemeier and Kevin Lehmann. *J. Phys. B*, 39:R127, 2006.
- [30] F. Dalfovo. *Zeitschrift für Physik D*, 29:61{66, 1994.
- [31] F. Ancilotto, G. DeTol, and F. Toigo. *Physical Review B*, 52:16125{16129, 1995.
- [32] F. Stienkemeier, J. Higgins, W. E. Ernst, and G. Scoles. *Physical Review Letters*, 74:3592{3595, 1995.
- [33] F. Stienkemeier, W. E. Ernst, J. Higgins, and G. Scoles. *Journal of Chemical Physics*, 102:615{617, 1995.
- [34] J. Higgins, C. Allegari, J. Reho, F. Stienkemeier, W. E. Ernst, M. Gutowski, and G. Scoles. *Journal of Physical Chemistry A*, 102:4952{4965, 1998.
- [35] J. P. Higgins. *Helium Cluster Isolation Spectroscopy*. PhD thesis, Princeton University, 1998.
- [36] J. P. Higgins, J. Reho, F. Stienkemeier, W. E. Ernst, K. K. Lehmann, and G. Scoles. *Spectroscopy in, on, and off a beam of superfluid helium nanodroplets*. In R. Campargue, editor, *Atomic and Molecular Beams: the state of the Art 2000*, pages 723{754. Springer, 2000.
- [37] F. Stienkemeier, J. Higgins, C. Allegari, S. I. Kanorsky, W. E. Ernst, and G. Scoles. *Zeitschrift für Physik D*, 38:253{263, 1996.
- [38] C. Allegari, J. Higgins, F. Stienkemeier, and G. Scoles. *Journal of Physical Chemistry A*, 102:95{101, 1998.
- [39] M. M. Udrich, O. Bunemann, F. Stienkemeier, O. Dulieu, and M. Weidemüller. *European Physical Journal D*, 31:291{299, 2004.
- [40] J. Reho, J. Higgins, and K. K. Lehmann. *Faraday Discussion*, 118:33{42, 2001.
- [41] T. Takayanagi and M. Shiga. *Chemical Physics Letters*, 372:90, 2003.
- [42] A. Braun and M. D. Rabbels. *Physical Review Letters*, 93:253401, 2004.
- [43] E. Logunov, D. Rossi, and M. D. Rabbels. *Physical Review Letters*, 95:163401, 2005.
- [44] S. Grebenev, J. P. Toennies, and A. F. V. Ilisov. *Science*, 279:2083{2085, 1998.
- [45] M. Hartmann, F. Mielke, J. P. Toennies, and A. F. V. Ilisov. *Physical Review Letters*, 76:4560, 1996.
- [46] J. Higgins, C. Allegari, J. Reho, F. Stienkemeier, W. E. Ernst, K. K. Lehmann, M. Gutowski, and G. Scoles. *Science*, 273:629{631, 1996.
- [47] C. P. Schulz, P. Claas, D. Schumacher, and F. Stienkemeier. *Physical Review Letters*, 92:013401, 2004.
- [48] S. Magnier and P. Mille. *Physical Review A*, 54:204, 1996.

- [49] A. M. Lyyra, T. T. Luh, L. Li, H. Wang, and W. C. Stwalley. *Journal of Chemical Physics*, 97:2, 1992.
- [50] M. Guhr, M. Bargheer, P. Dietrich, and N. Schwentner. *Journal of Physical Chemistry A*, 106:12002, 2002.
- [51] S. Vongehr and V. V. Kresin. *Journal of Chemical Physics*, 119:11124{11129, 2003.